The Astrophysical Journal, 909:154 (10pp), 2021 March 10 https://doi.org/10.3847/1538-4357/abddbd

X-Ray Pulsar XTE J1858+034: Discovery of the Cyclotron Line and the Revised Optical Identification

Sergey S. Tsygankov[1,2], Alexander A. Lutovinov[2], Sergey V. Molkov[2], Anlaug A. Djupvik[3,4], Dmitri I. Karasev[2], Victor Doroshenko[2,5], Alexander A. Mushtukov[2,6,7], Christian Malacaria[8,9], Peter Kretschmar[10], and Juri Poutanen[1,2,11]
[1] Department of Physics and Astronomy, FI-20014 University of Turku, Finland; sergey.tsygankov@utu.fi
[2] Space Research Institute of the Russian Academy of Sciences, Profsoyuznaya Str. 84/32, Moscow 117997, Russia
[3] Nordic Optical Telescope, Apartado 474, E-38700 Santa Cruz de La Palma, Santa Cruz de Tenerife, Spain
[4] Department of Physics and Astronomy, Aarhus University, NyMunkegade 120, DK-8000 Aarhus C, Denmark
[5] Institut für Astronomie und Astrophysik, Universität Tübingen, Sand 1, D-72076 Tübingen, Germany
[6] Leiden Observatory, Leiden University, NL-2300RA Leiden, The Netherlands
[7] Pulkovo Observatory, Russian Academy of Sciences, Saint Petersburg 196140, Russia
[8] NASA Marshall Space Flight Center, NSSTC, 320 Sparkman Drive, Huntsville, AL 35805, USA
[9] Universities Space Research Association, Science and Technology Institute, 320 Sparkman Drive, Huntsville, AL 35805, USA
[10] European Space Agency (ESA), European Space Astronomy Centre (ESAC), Camino Bajo del Castillo s/n, E-28692 Villanueva de la Caada, Madrid, Spain
[11] Nordita, KTH Royal Institute of Technology and Stockholm University, Roslagstullsbacken 23, SE-10691 Stockholm, Sweden
Received 2020 November 4; revised 2021 January 12; accepted 2021 January 18; published 2021 March 15

Abstract

We present the results of a detailed investigation of the poorly studied X-ray pulsar (XRP) XTE J1858+034 based on the data obtained with the NuSTAR observatory during the outburst of the source in 2019. The spectral analysis resulted in the discovery of a cyclotron absorption feature in the source spectrum at ∼48 keV in both the pulse phase-averaged and resolved spectra. Accurate X-ray localization of the source using the NuSTAR and Chandra observatories allowed us to accurately determine the position of the X-ray source and identify the optical companion of the pulsar. The analysis of the counterpart properties suggested that the system is likely a symbiotic binary hosting an XRP and a late-type companion star of the K-M classes rather than a Be X-ray binary as previously suggested.

Unified Astronomy Thesaurus concepts: Accretion (14); Stellar accretion disks (1579); Magnetic fields (994); Binary pulsars (153); Neutron stars (1108); High mass x-ray binary stars (733); X-ray binary stars (1811)

1. Introduction

The transient X-ray pulsar (XRP) XTE J1858+034 was discovered with the All Sky Monitor (ASM) on board the RXTE observatory in 1998 (Remillard et al. 1998). Pulsations with a period of 221.0 ± 0.5 s detected during the same outburst in the RXTE/PCA data (Takeshima et al. 1998) and the transient nature of XTE J1858+034 led these authors to conclude that the system is likely an XRP with a Be counterpart. A long-term light curve based on the RXTE/ASM data clearly shows regular outbursts with a period of ∼380 days, which was interpreted as the orbital period of the binary system (Doroshenko et al. 2008).

The energy spectrum of XTE J1858+034 is typical for XRPs and can be described as an absorbed cutoff power law with an equivalent hydrogen column density of 6×10^{22} cm^{-2}, modified by an iron emission line around 6.6 keV (Paul & Rao 1998). A similar spectral shape and parameters were obtained from INTEGRAL data (Filippova et al. 2005; Doroshenko et al. 2008) collected during an outburst in 2004 (Molkov et al. 2004). Evidence of a cyclotron absorption line has never been reported for XTE J1858+034 in the literature; therefore, the magnetic field strength of the neutron star (NS) remains uncertain. On the other hand, Paul & Rao (1998) discovered quasiperiodic oscillations at 0.11 Hz, which is significantly higher than the spin frequency. Interpreting this feature in the frame of the beat frequency model, they estimated the NS magnetic field to be $0.8 \times 10^{12} r_{\rm kpc}$ G, where $r_{\rm kpc}$ is the distance to the system in kiloparsecs.

The X-ray localization of XTE J1858+034 was originally obtained from the RXTE data (Marshall et al. 1998) and later improved by Molkov et al. (2004) using the observations with INTEGRAL/JEM-X and INTEGRAL/IBIS/ISGRI. Based on these results, Reig et al. (2005) proposed a star with the coordinates R.A. $= 18^{\rm h}58^{\rm m}36^{\rm s}$, decl. $= 3°26'09''$ as a possible counterpart for the source. Optical spectroscopy indicated that it was the only nearby star exhibiting Hα emission; however, its position was not consistent with the JEM-X uncertainty. Therefore, this association can only be considered tentative.

The relative faintness of XTE J1858+034 even during its outbursts and shortage of available data did not allow for making any definitive conclusions regarding the physical properties of the NS in the system to date. Here we report the results of a NuSTAR observation of XTE J1858+034 performed during its outburst in the fall of 2019 (detected by the MAXI instrument; Nakajima et al. 2019), which allowed for conducting a detailed spectral and timing analysis and localizing the source. The localization of the source was then further refined using an archival Chandra observation and subsequent near-IR identification of the companion star using the Nordic Optical Telescope (NOT) telescope.

2. Observations and Data Reduction

This work is based on several data sets in the X-ray (Chandra, XMM-Newton, and NuSTAR observatories) and near-IR (the UKIDSS survey and NOT) bands. The complete list of the data used is presented in Table 1.

2.1. NuSTAR Observatory

The NuSTAR observatory includes two identical coaligned X-ray telescopes focusing X-ray photons onto two focal plane modules, A and B (FPMA and FPMB; Harrison et al. 2013). In

Table 1
List of XTE J1858+034 Observations Utilized in This Work

ObsID	Start Date	Start MJD	Exposure (ks)
	XMM-Newton		
0302970201	2006-04-11	53,836.91	25
	Chandra		
14645	2013-02-17	56,340.17	5
	NuSTAR		
90501348002	2019-11-03	58,790.29	43
	NOT		
STzd200003-7	2016-04-21	57,499.11	0.12[a]
NCzd200587-640	2016-04-21	57,499.11	0.54[b]
NCzi150446-449	2016-09-15	57,646.99	2.4

Notes.
[a] Per filter *BVRi*.
[b] Per filter JHK_s.

the context of the current work, the most important NuSTAR capabilities are the moderately high imaging resolution of 18″ (FWHM) and unprecedented sensitivity in hard X-rays from 3 to 79 keV. The XRP XTE J1858+034 was observed with NuSTAR on 2019 November 3 with an exposure of ∼43 ks (see Table 1) near the peak of the outburst.

The raw data were reduced following the standard procedures described in the NuSTAR user guide and using the standard NuSTAR Data Analysis Software (NUSTARDAS) v1.8.0 with CALDB version 20190513. The source spectrum was extracted from a source-centered circular region with a radius of 80″ using the NUPRODUCTS routine. The background was extracted from a source-free circular region with a radius of 80″ in the corner of the field of view. In order to apply standard χ^2 minimization procedures, the original source spectrum was rebinned in order to have at least 25 counts per energy bin. The following spectral analysis was performed using the XSPEC package (Arnaud 1996).

2.2. XMM-Newton Observatory

In order to investigate different states of XTE J1858+034, the XMM-Newton data obtained during the quiescent state of the source were also analyzed. The source was observed in 2006 April for ∼25 ks. The EPIC pn and MOS detectors were operated in the full-frame mode with medium filters. The data reduction procedures using the XMM-Newton Science Analysis Software (SAS; version 18.0) were applied following standard procedures.[12] After the standard pipeline processing, we searched for possible intervals of high background and rejected them. This resulted in lowering the effective exposure down to ∼16 and ∼6 ks for MOS and pn, respectively. For the analysis of the EPIC data, we selected events with patterns in the range 0–4 for the pn camera and 0–12 for the two MOS cameras, using a circular region with a radius of 20″ around the source positions. The circular background region with a radius of 30″ was placed close to the source at the same CCD and avoiding other point sources.

2.3. Chandra Observatory

The XRP XTE J1858+034 was observed by the Chandra Advanced CCD Imaging Spectrometer (ACIS; Garmire et al. 2003) on 2013 February 17 with an exposure of ∼5 ks as part of the project aimed at studies of the transient XRPs in a quiescent state (Tsygankov et al. 2017b). For the data reduction, we used the software package CIAO v4.12 with an up-to-date CALDB v4.9.1. The procedure CELLDETECT was used to determine the coordinates of the sources in the Chandra field of view. The source spectrum was extracted from a circular aperture with a radius of 3″ around the position, while for the background extraction, we used a circular region near the source with a radius of 15″.

2.4. Nordic Optical Telescope

Optical and near-IR observations were obtained at the NOT through applications in the fast-track service (Djupvik & Andersen 2010) using the standby CCD camera StanCam and the NOT near-IR camera and spectrograph (NOTCam[13]). StanCam images in the *BVRi* bands, as well as NOTCam high spatial resolution images (0.″079 pixel^{-1}) in the JHK_s bands, were obtained on 2016 April 20 in good seeing conditions (FWHM = 0.″6–0.″7). The near-IR images were obtained by small step dithering in a 3 × 3 pattern with 30 s exposures in each position obtained in ramp-sampling mode, reading out every 5 s, giving a total of 540 s filter^{-1} in the combined *J*, *H*, and K_s images. The StanCam exposures of 120 s showed no detection in any band, while the near-IR images detected a red counterpart at the location of the X-ray source. A *K*-band spectrum was obtained on 2016 September 15 under less favorable conditions. The setup used was the WF camera (0.″234 pixel^{-1}), grism 1 with a dispersion of 4.1 Å pixel^{-1}; the 128 μm slit (0.″6 wide); and the *K*-band filter (number 208) used as an order sorter, which gives a resolution of 10.5 Å and resolving power of $\lambda/\Delta\lambda = 2100$. The spectra were obtained in the ABBA dithering mode, exposing 600 s position^{-1} and using the ramp-sampling mode to read out nondestructively 10 times every 60 s. In situ arc and halogen lamps were observed to take out the effect of fringing as much as possible and account for flexure in the wavelength calibration. A telluric standard close to the target was observed immediately before the target.

The near-IR images were reduced using the NOTCam IRAF package to do bad-pixel correction, flat-fielding with differential twilight flats, sky subtraction, and shifting and median combining of the individual images. The individual 2D *K*-band spectra were hot- and zero-pixel-corrected, flat-fielded, and sky-subtracted before 1D extraction using standard IRAF tasks. The individual 1D spectra were wavelength-calibrated and thereafter combined into a final spectrum. This was divided by the telluric standard spectrum to correct for atmospheric features and afterward multiplied by a blackbody continuum of the same spectral type as the telluric standard to correct the slope in the spectrum. Due to mediocre sky conditions, the final spectrum had a poor S/N ratio and was therefore smoothed over 17 pixels, lowering the resolving power to $R = 120$.

3. Results

The XRP XTE J1858+034 was observed by the NuSTAR observatory close to the peak of the 2019 outburst. The light curve of the source in the 15–50 keV energy band obtained[14] by the Burst Alert Telescope on board the Neil Gehrels Swift Observatory (Swift/BAT; Krimm et al. 2013) is shown in

[12] https://www.cosmos.esa.int/web/xmm-newton/sas-threads

[13] For details about NOTCam, we refer to http://www.not.iac.es/instruments/notcam/.

[14] http://swift.gsfc.nasa.gov/results/transients/

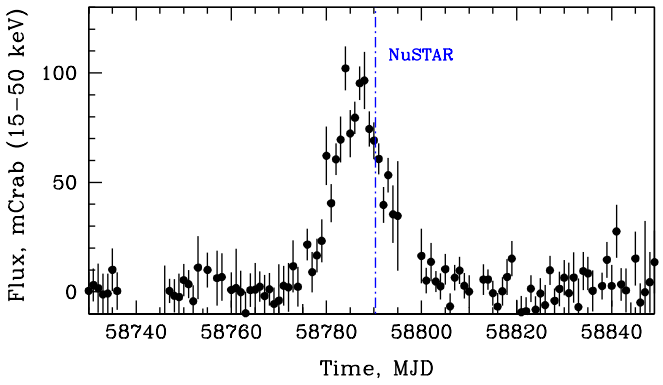

Figure 1. Light curve of XTE J1858+034 in the 15–50 keV energy band obtained by the Swift/BAT monitor. The vertical dashed–dotted line corresponds to the time of our NuSTAR observation.

Figure 1. The relatively high brightness of the source allowed us to study its properties in a broad energy band in detail. At the same time, soft-band Chandra and XMM-Newton data were collected in the low state with low counting statistics that were insufficient to detect pulsations. All uncertainties in the paper are reported at a 1σ confidence level, unless otherwise stated.

3.1. Pulse Profile and Pulsed Fraction

Orbital parameters, except for the orbital period, are not known for XTE J1858+034. Considering that the available X-ray data only cover a small fraction of the orbit, it was also impossible to determine those based on the X-ray timing. Therefore, for the timing analysis, only the barycentric but no binary correction was applied to the light curves. Using a standard epoch folding technique (EFSEARCH task of FTOOLS; Leahy 1987), strong pulsations in the full band were found with the period $P = 218.382(2)$ s. The uncertainty for the pulse period value was determined from the simulated light curves following the procedure described by Boldin et al. (2013).

High count statistics allowed us to reconstruct the pulse profile of the source in several energy bands (selected to provide a sufficient number of photons in each) from 3 to 79 keV (see Figure 2). Even at the highest energies (in the 40–80 keV band), where counting statistics are limited, pulsations at an expected period are significantly detected in a blind search (Lomb–Scargle false-alarm probability $p \sim 2.8 \times 10^{-7}$ for over 2.5 million trial periods). The overall shape of the pulse profile is sine-like single-peaked, consistent with the results from the INTEGRAL observatory obtained by Doroshenko et al. (2008). We note, however, that although the pulse profile shape remains constant at different energies, some tentative sign of a phase lag is observed, with the soft profile lagging the hard one.

Based on the energy-resolved pulse profiles with 12 phase bins, we also calculated the pulsed fraction[15] as a function of energy presented in Figure 3. The linear increase of the pulsed fraction toward higher energies can be clearly seen, which is consistent with the typical behavior of most XRPs (Lutovinov & Tsygankov 2009).

3.2. Phase-averaged Spectral Analysis

Previously, the spectral properties of XTE J1858+034 in the X-ray band were studied using RXTE and INTEGRAL data

[15] Here $PF = (F_{max} - F_{min})/(F_{max} + F_{min})$, where F_{max} and F_{min} are the maximum and minimum fluxes in the pulse profile, respectively.

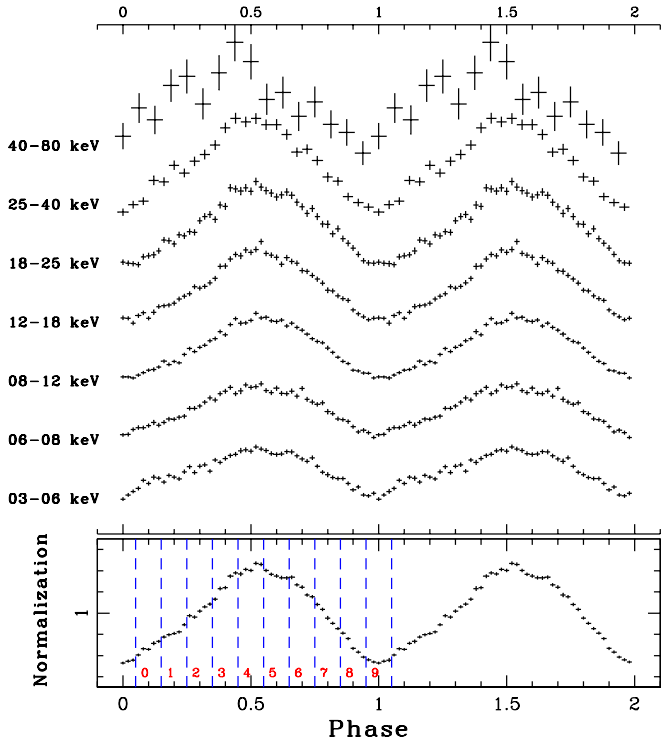

Figure 2. Top: pulse profiles of XTE J1858+034 obtained with NuSTAR in different energy bands. The profiles are shown twice in phase and arbitrarily rescaled in count rate for clarity. Bottom: pulse profile of XTE J1858+034 in the full energy band 3–79 keV with phase bins selected for the phase-resolved spectral analysis shown with vertical dashed lines.

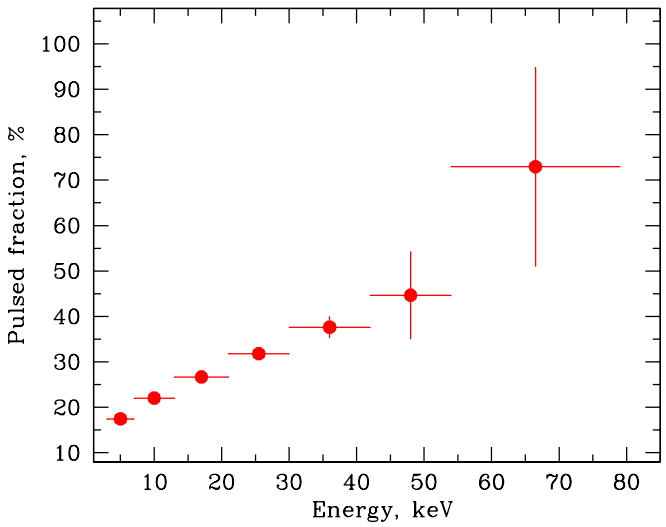

Figure 3. Dependence of the pulsed fraction of XTE J1858+034 on energy based on the NuSTAR data.

(Paul & Rao 1998; Filippova et al. 2005; Doroshenko et al. 2008). In both cases, it was concluded that the source spectrum can be fit with an absorbed power law with a high-energy exponential cutoff, i.e., the typical spectrum for XRPs. No evidence for other features, such as cyclotron lines, was reported. The NuSTAR observatory, owing to a sufficiently high-energy resolution and much better sensitivity at high energies, allowed us to conduct a much more detailed search for the possible cyclotron lines in the source spectrum.

Similarly to RXTE and INTEGRAL, the NuSTAR spectrum below ~40 keV can be well described with several continuum

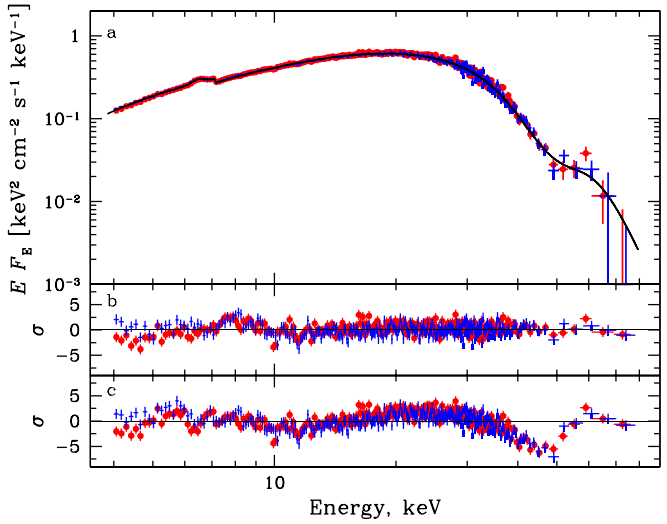

Figure 4. (a) Unfolded X-ray spectrum of XTE J1858+034 obtained with the NuSTAR observatory. The data from the FPMA and FPMB modules are shown in red and blue, respectively. The solid black line represents the best-fit model. (b) Residuals from the best-fit model for the NuSTAR data. (c) Residuals from the best-fit model not including the cyclotron absorption line.

Table 2
Best-fit Parameters for a PHABS × (GAU + COMPTT) × GABS Model Obtained for the NuSTAR Observation

Parameter	Units	Value
$N_{\rm H}$	10^{22} cm^{-2}	7.5 ± 0.3
$E_{\rm Fe}$	keV	6.47 ± 0.02
$\sigma_{\rm Fe}$	keV	0.22 ± 0.03
$N_{\rm Fe}$	10^{-4} ph cm^{-2} s^{-1}	4.4 ± 0.5
T_0[a]	keV	1.0[a]
T[b]	keV	5.63 ± 0.01
τ[c]	⋯	6.58 ± 0.01
$E_{\rm cyc}$	keV	47.7 ± 0.2
$\sigma_{\rm cyc}$	keV	8.15 ± 0.13
Strength$_{\rm cyc}$	⋯	20.6 ± 0.5
$C_{\rm FPMA/FPMB}$[d]	⋯	1.013 ± 0.002
Flux[e]	10^{-9} erg s^{-1} cm^{-2}	$1.7s^{+0.4}_{-0.6}$
χ^2 (dof)	⋯	1909.3 (1682)

Notes.
[a] Input soft photon temperature, 3σ upper limit.
[b] Plasma temperature.
[c] Plasma optical depth.
[d] Cross-normalization factor between two NuSTAR modules.
[e] Unabsorbed flux in the 3–100 keV energy band.

models. In particular, we attempted to fit the data with several phenomenological continuum models commonly used for XRPs, i.e., the Comptonization model (COMPTT in XSPEC) and a power law with a high-energy exponential cutoff (CUTOFFPL or PO × HIGHECUT in XSPEC). A more detailed study of different phenomenological and physical models applied to the source spectrum is presented in the accompanying paper by Malacaria et al. (2021).

To get an adequate fit, photoelectric absorption at low energies (PHABS in XSPEC, assuming the standard solar abundance from Anders & Grevesse 1989) and a fluorescent iron emission line (GAU in XSPEC) were introduced to the model. However, irrespective of the continuum model we used, residuals around ∼45 keV in absorption are also immediately apparent in the phase-averaged spectrum of XTE J1858+034. Figure 4 demonstrates the case of the COMPTT continuum model (see panel (c)), but similar residuals also appear with other models. The fit can be greatly improved by inclusion of a Gaussian absorption line in the model (Figure 4(b)). The best-fit spectral parameters are presented in Table 2. Inclusion of an absorption line with energy 47.7(2) keV improves the fit from $\chi^2/{\rm dof} = 2926.8/1685$ to $\chi^2/{\rm dof} = 1909.3/1682$. The high statistical significance of the feature is obvious from the huge $\Delta\chi^2$ value. Its proper estimate using the XSPEC script SIMFTEST is technically infeasible due to an unrealistically large number of required simulations (the largest χ^2 change obtained in 10^4 simulations was only 48, which allows us to conclude that the significance estimated using this method must be high and, in any case, more than 3σ). Applying the F-test, we calculated a false-detection probability for the line of $P = 2.0 \times 10^{-155}$.

The detection of a cyclotron line at ∼48 keV implies a magnetic field in XTE J1858+034 of $\sim 5.2 \times 10^{12}$ G, assuming a gravitational redshift $z = 0.26$ for the typical NS parameters ($R = 12$ km and $M = 1.5\ M_\odot$). Applying the CYCLABS model instead of GABS to describe the line results in a lower cyclotron energy of ∼44 keV. The discrepancy between these two models is related to their definition and was found in other studies (e.g., Nakajima et al. 2010; Mushtukov et al. 2015b; Doroshenko et al. 2017); see also the discussion of different line models in the review of Staubert et al. (2019). We emphasize only that it should be kept in mind when comparing results from different studies.

In the quiescent state, XTE J1858+034 was observed twice: in 2006 April with XMM-Newton and 2013 February with Chandra. In both cases, the source was found in the very low state with the flux about 3 orders of magnitude lower than in our NuSTAR observation. Both spectra were fitted with an absorbed power law (PHABS × POW in XSPEC) and blackbody (PHABS × BB in XSPEC) in order to determine the origin of the source emission in quiescence. A systematic study of the quiescent emission in transient XRPs with Be optical companions was conducted by Tsygankov et al. (2017b); however, XTE J1858+034 was excluded from their sample due to the uncertain nature of its optical counterpart.

Taking into account the small number of collected photons, the spectra in the low state were binned to have at least one count in each energy channel and fitted using the W-statistics (Wachter et al. 1979). For the same reason, it was impossible to constrain the absorption column simultaneously with other parameters. Therefore, we fixed it at the best-fit value obtained from the NuSTAR data ($N_{\rm H} = 7.5 \times 10^{22}$ cm^{-2}). The best-fit spectral parameters in the soft X-ray band are presented in Table 3. It is clear that both models can fit the data equally well.

We also fitted XMM-Newton MOS and pn data jointly using the same simple models but with $N_{\rm H}$ as a free parameter in order to check if the absorption value depends on the luminosity state of the source. As a result, for the blackbody model, we obtained $N_{\rm H} = (1.8^{+1.7}_{-1.1}) \times 10^{22}$ cm^{-2} and temperature $kT = 2.1^{+0.8}_{-0.5}$ keV; for the power law, we obtained $N_{\rm H} = (3.8^{+2.6}_{-2.0}) \times 10^{22}$ cm^{-2} and photon index $0.9^{+0.7}_{-0.6}$. With a similar quality of the fit, we cannot make any final conclusions on the possibility of lower absorption in the quiescent state.

Table 3
Best-fit Parameters for the PHABS × POW and PHABS × BB Models Obtained for Both Observations in the Low State

Parameter	Chandra	XMM-Newton
PHABS × POW Model		
$N_{\rm H}$ (10^{22} cm^{-2})	$7.5^{\rm fix}$	
Γ	-0.4 ± 0.7	1.7 ± 0.9
C-value (dof)	27.5 (23)	105.5 (119)
Flux[a] (erg s^{-1} cm^{-2})	$4.2^{+0.2}_{-2.7} \times 10^{-13}$	$4.3^{+0.3}_{-3.1} \times 10^{-13}$
PHABS × BB Model		
$N_{\rm H}$ (10^{22} cm^{-2})	$7.5^{\rm fix}$	
$kT_{\rm bb}$ (keV)	$2.3^{+1.8}_{-0.7}$	$1.4^{+0.6}_{-0.4}$
C-value (dof)	27.4 (23)	104.9 (119)
Flux[a] (erg s^{-1} cm^{-2})	$3.5^{+0.3}_{-1.6} \times 10^{-13}$	$2.8^{+0.4}_{-0.9} \times 10^{-13}$

Note.
[a] Unabsorbed flux in the 0.5–10 keV energy band.

Both Chandra and XMM-Newton observed XTE J1858+034 shortly after the flares and measured hard spectra (i.e., both have low photon indexes or high blackbody temperatures) and fluxes. The hard spectral shape points to a likely nonthermal origin of the emission (Tsygankov et al. 2017b). The source exhibits regular outburst activity, and persistent accretion between flares cannot be excluded. Moreover, owing to the long spin period, XTE J1858+034 may belong to the group of pulsars accreting from a cold low-ionized disk even in a quiescent state (Tsygankov et al. 2017a).

3.3. Phase-resolved Spectral Analysis

The high counting statistics of the NuSTAR data allowed us to perform a pulse phase-resolved spectral analysis. For that, we used our best-fit model from the phase-averaged spectroscopy (PHABS × (GAU + COMPTT) × GABS) and the phase binning shown in Figure 2, which was defined based on the available counting statistics and observed pulse profile morphology. The source spectral parameter variations over the pulse are shown in Figure 5. Based on the SIMFTEST simulations, the significance of the cyclotron line in all phase-resolved spectra was shown to be higher than 3σ.

We see that the continuum parameters (temperature and optical depth of the Comptonizing plasma) vary significantly, whereas the relatively large uncertainty on the cyclotron line parameters prevent us from making any conclusion on their stability. The fitted values for the absorption column, iron line parameters, and temperature of the seed photons stay constant within the errors over the pulse.

3.4. X-Ray Position

The original localization accuracy of XTE J1858+034 obtained with the RXTE observatory was 6′ (Remillard et al. 1998). This was further improved by Marshall et al. (1998) based on repeated scans across the source with the RXTE/PCA instrument, which allowed to localize the source at R.A.(2000) = $18^{\rm h}58^{\rm m}.6$, decl. (2000) = 3°21′, with a 90% confidence error radius of 2.′5. Later, using the imaging capabilities of the JEM-X and IBIS telescopes on board the INTEGRAL observatory, Molkov et al. (2004) further constrained the coordinates of XTE J1858+034 as

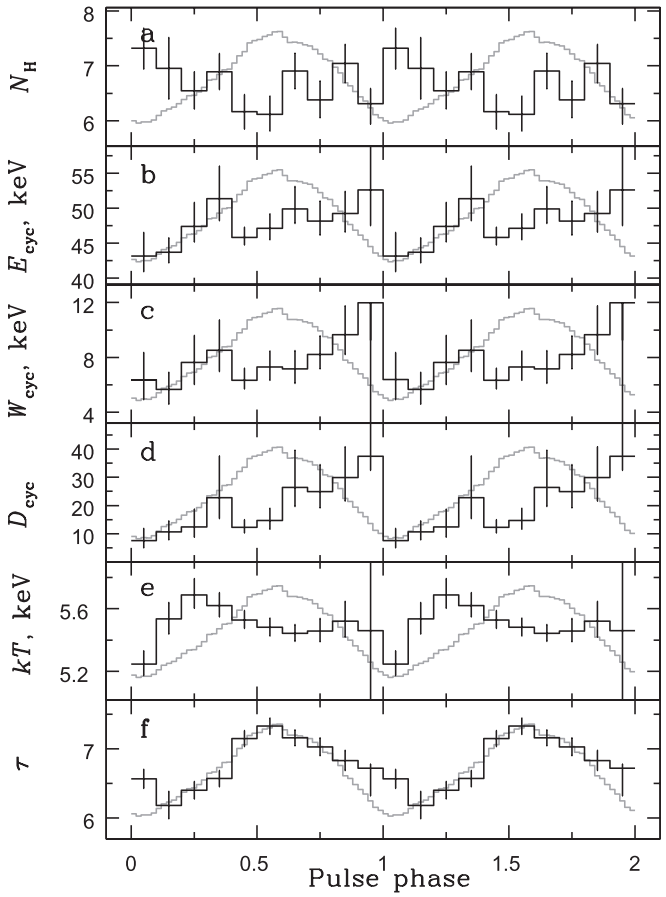

Figure 5. Dependence of the spectral parameters of XTE J1858+034 on the pulse phase revealed from the NuSTAR data. Different panels correspond to the absorption column in units of 10^{22} cm^{-2} (a), cyclotron line energy (b), width (c), strength (d), Comptonizing plasma temperature (e), and optical depth (f). The pulse profile in the 3–79 keV energy band is shown in gray for clarity.

R.A. = $18^{\rm h}58^{\rm m}43^{\rm s}$, decl. = 3°26′06″ for the IBIS/ISGRI data with the 2′ uncertainty and R.A. = $18^{\rm h}58^{\rm m}44^{\rm s}$, decl. = 3°26′02″ for the JEM-X data with the 1′ uncertainty. The X-ray image of the sky field obtained with the Chandra observatory is shown in Figure 6. Two weak X-ray sources compatible with these localization regions were found in the data.

In order to determine the nature of XTE J1858+034, Reig et al. (2005) performed optical photometric and spectroscopic observations of the field around the best-fit INTEGRAL position. It was revealed that only one star with the coordinates R.A. = $18^{\rm h}58^{\rm m}36^{\rm s}$, decl. = 3°26′09″ exhibits Hα emission (marked with a white plus sign in Figure 6). This star was proposed to be a possible counterpart of XTE J1858+034, since the counterpart was expected to be a Be star.

However, Figure 6 demonstrates that this star cannot be an optical companion of XTE J1858+034 (source marked with the number 1). This conclusion is confirmed by at least three facts: coincidence of the localization regions obtained by INTEGRAL/JEM-X and NuSTAR (see green contours in Figure 6), detection of X-ray pulsations with a period of ∼221 s by NuSTAR, and coincidence of the NuSTAR and Chandra positions.

Using our Chandra data, we obtained the precise coordinates for XTE J1858+034 of R.A. = $18^{\rm h}58^{\rm m}43^{\rm s}.64$, decl. = 3°26′05.″8 (J2000, marked with the number 1 in Figure 6) using the WAVDETECT tool from the CIAO package. A statistical uncertainty

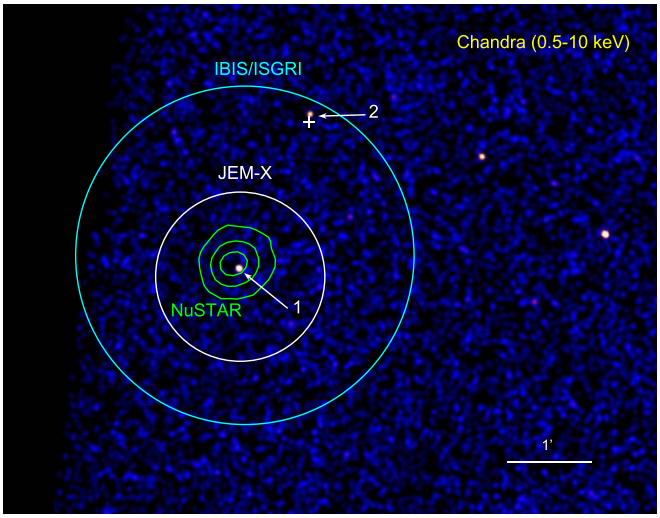

Figure 6. Image of the sky field near XTE J1858+034 obtained with the Chandra observatory in the 0.5–10 keV energy band. Localization uncertainties obtained from INTEGRAL/JEM-X and IBIS/ISGRI are shown with white and cyan circles, respectively. Green equal-flux contours represent the NuSTAR data analyzed in this work. Numbers 1 and 2 correspond to the possible X-ray counterparts consistent with the IBIS/ISGRI localization (see the text). A white plus sign marks the position of the optical counterpart proposed by Reig et al. (2005).

of 0.″8 at the 90% confidence level was obtained following the recommendations available on the online threads.[16] Taking into account the systematic uncertainty of the Chandra absolute positions of the same value,[17] the resulting localization accuracy of the source we obtained is 1.″2 (90% confidence level radius; see blue circle in Figure 7).

4. Discussion

4.1. Structure of the Emitting Region

The observational properties of X-ray emission from XRPs depend on the physical conditions and geometrical structure of the emitting regions at the NS surface and thus can be used to probe them. As was already mentioned in Section 3.1, the pulse profile of XTE J1858+034 has a sine-like single-peaked shape that is almost independent of energy. At the same time, some tentative sign of a phase lag is observed, with the soft profile lagging the hard one. A quantitative interpretation of this phenomenon is not possible in the absence of adequate models describing the emission of XRPs; however, qualitatively, one may speculate that it may be associated with the resonant scattering of X-ray photons by the accretion flow above the hot spot. Indeed, considering that the source is likely in the subcritical regime of accretion (see below), the optical thickness of the accretion flow above the hot spot is below unity for a nonresonant scattering. Thus, the low-energy photons ($E < 25$ keV) leave the system freely with a pencil-beam emission diagram (Basko & Sunyaev 1975). However, the scattering cross section near the cyclotron energy ($E_{\rm cyc} = 48$ keV; see below) is well above unity (Herold 1979; Daugherty & Harding 1986). Because of that, the cyclotron photons are scattered by the accretion flow. This results in an energy-dependent beam function, leading to the observed lag between the pulse profiles.

[16] https://cxc.harvard.edu/ciao/threads/wavdetect/
[17] https://cxc.harvard.edu/cal/ASPECT/celmon/

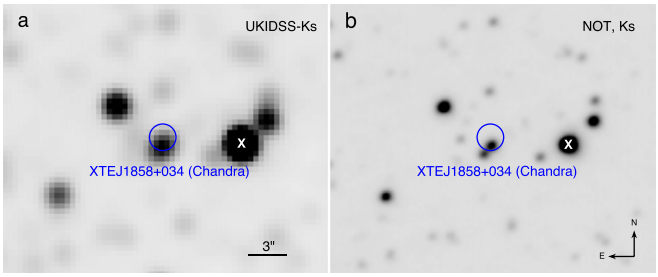

Figure 7. Images of the sky containing XTE J1858+034 obtained in the K band from the GPS/UKIDSS sky survey data (left) and the NOT (right). The blue circle indicates the Chandra observatory error circle for the source position. The cross indicates the star previously considered by Malacaria et al. (2020) as a possible companion.

Variations of the spectral continuum over the pulse phase are also consistent with a pencil-beam emission diagram. From Figure 5, one can also notice that the optical depth τ appears to correlate with the flux in the profile, whereas the plasma temperature kT shows an anticorrelation (except main minimum around zero phase) reaching maximum values in the wings of the flux peak (see Figure 5(e)). This behavior can be interpreted in terms of the subcritical accretion onto a strongly magnetized NS with a pencil-beam emission diagram. In this case, the accretion flow loses its kinetic energy in the atmosphere of an NS, resulting in the inverse temperature profile in the NS atmosphere with hotter upper layers where most of energy is released (Basko & Sunyaev 1975). The maximal flux in the pulse profile corresponds to the situation when an observer looks at a hot spot close to the local normal. Then, photons from the deeper and colder layers are detected, resulting in a negative/positive correlation of temperature/optical depth with the photon energy flux. This result points to a pencil-beam pattern for the pulsars operating in a subcritical regime. The estimated luminosity of XTE J1858+034 during our NuSTAR observation is $L \sim 2 \times 10^{37}$ erg s^{-1} for a distance of 10 kpc (see below), whereas the critical luminosity for the pulsar with magnetic field $B \sim 5 \times 10^{12}$ G is expected to be around 3×10^{37} erg s^{-1} (Mushtukov et al. 2015a). Thus, one may conclude that XTE J1858+034 was observed very close to the critical luminosity but still in the subcritical regime.

4.2. Origin of the IR Companion

The study of optical catalogs and observational data showed the absence of any object in the localization region of the X-ray source. The upper limit on the observed magnitudes in filters g, r, and i, according to the Pan-STARRS instrumental filters, is around 23.1.

Inspecting the UKIDSS catalog,[18] we found that the position of XTE J1858+034 determined from the Chandra data is compatible with a faint infrared star, which, in turn, is apparently blended with another one (Figure 7(a)). The blue circle illustrates an uncertainty of the source X-ray position. Based on the UKIDSS data, it is impossible to separate the fluxes from these stars to measure the correct magnitudes of the counterpart in the near-IR bands. Therefore, to measure the characteristics of the counterpart of XTE J1858+034, we performed observations with the NOT in several filters ($BVRiJHK_s$). The image of the sky field around XTE J1858+034 obtained with NOTCam in the K_s filter is shown in

[18] http://wsa.roe.ac.uk/

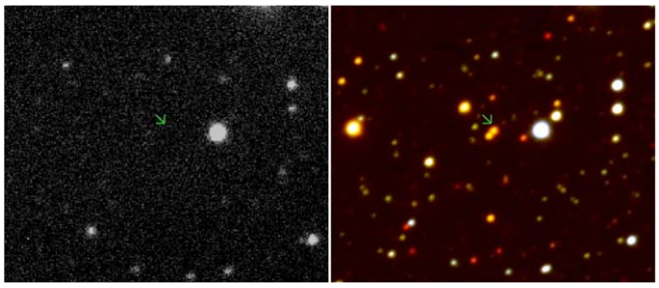

Figure 8. Left: StanCam *i*-band image with exposure of 120 s. Right: NOTCam JHK_s color-coded image, each 540 s. The green arrow shows the IR companion of XTE J1858+034. Both have N up and E left and show the same region.

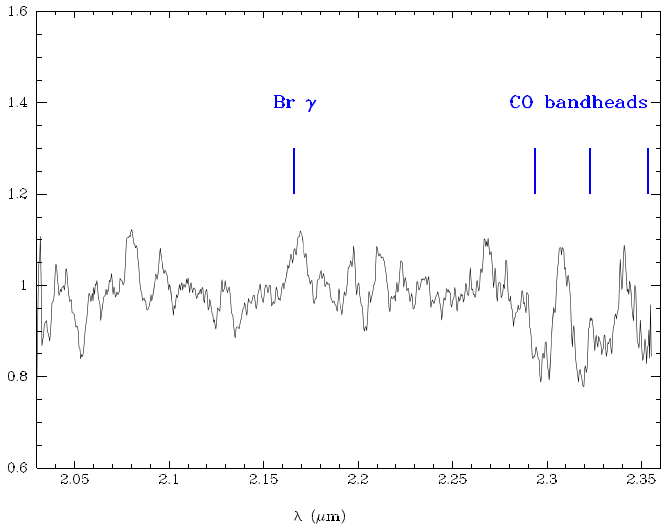

Figure 9. The *K*-band spectrum of the IR counterpart of XTE J1858+034. The locations of the CO 2–0, 3–1, and 4–2 band heads at 2.29, 2.32, and 2.35 μm are indicated.

Figure 7(b). It is clearly seen that the two objects are perfectly separated by a distance of 0.″7; thus, the only infrared companion of the source in the NOTCam data is a star with the coordinates of R.A. $= 18^{\rm h}58^{\rm m}43\overset{\rm s}{.}63$, decl. $= 3°26'05.''2$ (J2000).

The StanCam *BVRi* images obtained at the NOT in good seeing show no detection at the location; see the *i*-band image compared to the JHK_s color image in Figure 8. Photometric analysis of the NOT data using point-spread function photometry (DAOPHOT II) allowed us to determine the magnitudes of this star as $J = 18.559 \pm 0.037$, $H = 15.291 \pm 0.035$, and $K = 13.520 \pm 0.027$. Note that, for calibrating instrumental magnitudes JHK_s and converting them into *JHK* ones, we used the GPS/UKIDSS catalog as a reference.

The *K*-band spectrum obtained with NOTCam resulted in a very low S/N ratio of around 7 due to less than optimal conditions. Smoothing the spectrum over 17 pixels, however, and thereby lowering the resolving power from 2100 to 120, improved the S/N to 20 and revealed a tentative detection of the CO 2–0, 3–1, and 4–2 band heads in absorption at 2.29, 2.32, and 2.35 μm, respectively, of which the latter is cut halfway by the instrument sensitivity; see Figure 9. The rms in the smoothed spectrum is of the order of 5%, and the depth of the features is around 15%, giving a 3σ detection. As shown in the *K*-band spectral catalog of Wallace & Hinkle (1997), the presence of these CO bands in absorption strongly suggests a late spectral type of luminosity class I or III.

The equivalent width estimate for the 2–0 band head at 2.297 μm is 24 Å, which would point to a late M-type giant or early M-type supergiant according to the relation between spectral type and CO equivalent widths in Figure 2 in Davies et al. (2007). The 3–1 band head at 2.323 μm is even broader but also more contaminated with noise. We believe it is fairly safe to deduce that the object is a late type, most likely an M-type giant or supergiant. The rest of the spectrum remains featureless, although there is a small bump below detection levels at the position of Brγ.

Some conclusions can also be made about the nature of the studied star based on the photometric results. Taking the intrinsic colors $(H-K)_0$ of different classes of stars from Wegner (2014, 2015), we compare them with the $(H-K)$ color of the counterpart determined from the NOT observations. From a simple relation $E(H-K) = (H-K) - (H-K)_0$, we can find an extinction correction for each class of stars to correspond to the measured color of the source. Assuming a standard extinction law (Cardelli et al. 1989) expected in this sky region, we can transform each $E(H-K)$ into A_K. At the same time, comparing absolute magnitudes in the *K* band of the same stars (Wegner 2000, 2006, 2007) with the measured magnitude of the source in the *K* band (taking into account A_K), we can estimate a probable distance to each class of stars from a relation $5\text{–}5\log_{10}D = M_{\rm K,abs} - K_{\rm NOT} + A_K$.

The results of such estimations for different classes of stars are presented in Figure 10. From this diagram, it is not possible to unambiguously determine the class of the companion, but we can get some restrictions on the extinction magnitude toward the source. In particular, for OB giants or supergiants, the extinction A_K toward XTE J1858+034 should be ∼(3.1–3.4); for red giant stars, $A_K \simeq (2.6\text{–}3.0)$; and for main-sequence stars, A_K is somewhere between these values. In particular, if we assume that the optical counterpart of XTE J1858+034 is a giant star, it should be located at ∼4–14 kpc from the Sun. Note that the above extinction converted into the hydrogen column density $N_{\rm H}$ via standard relations (Predehl & Schmitt 1995; Güver & Özel 2009) generally agrees with the results obtained from the source X-ray spectrum in the low state.

A significant absorption toward the source can easily explain its nondetection in optical filters at the NOT and with Gaia. The extinction $A_K \simeq 2.8$ corresponds to $A_i \simeq 16$ for the standard law. Thus, an expected magnitude of the source in the *i* filter should be ∼30.

At the next step, we compare the observed colors $(J-K)$ and $(J-H)$ of the counterpart with the intrinsic ones of different classes of stars in a similar way as described by Karasev et al. (2012). The red dots in Figure 11 indicate the colors of the different types of stars in the nearest 100 pc from the Sun taken from the Two Micron All Sky Survey (2MASS) catalog and Hipparcos observatory data (van Leeuwen 2007). The interstellar extinction for such nearby stars in the IR filters is negligibly small, so we obtain the desired set of unabsorbed reference stars of different classes. The lines at the bottom indicate the regions of the diagram corresponding to a particular type of star (marked by the letters; see, e.g., Wegner 2014, 2015).

The position of the IR counterpart of XTE J1858+034 ($J-H \simeq 3.27$ and $J-K \simeq 5.04$) is far beyond this diagram due to a significant interstellar extinction (see Figure 12). But, by correcting the source's magnitudes for different extinctions, we

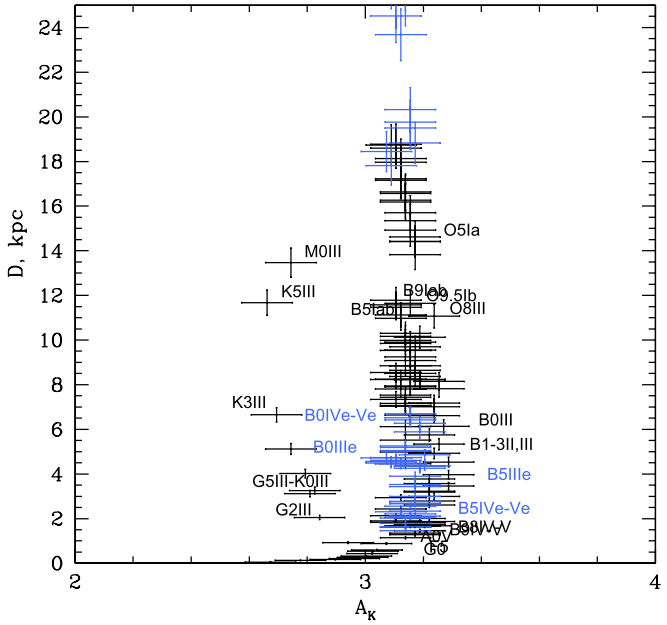

Figure 10. Distance–absorption diagram showing how far a star of a specific class should be located if it is a counterpart of XTE J1858+034 and the appropriate magnitude of the absorption toward such a star. A subclass of Be stars is marked in blue.

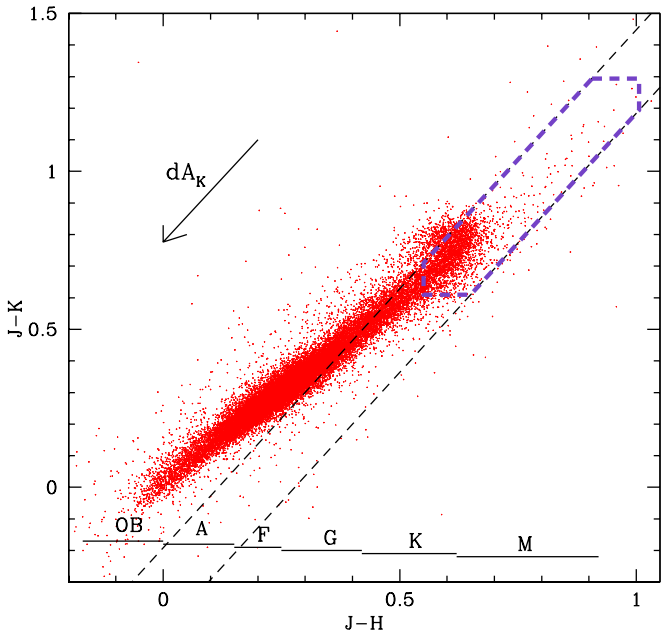

Figure 11. Color–color diagram for unreddened stars (2MASS+Hipparcos) of various spectral types (marked by the lines with the letters of the spectral types). The inclination of the arrow corresponds to a standard extinction law (Cardelli et al. 1989). Dashed lines track the variation of the colors of the counterpart of XTE J1858+034 due to variation of the absorption correction. The violet polygon marks the most probable class of stars to be a real counterpart of the source.

can shift its colors downward and to the left toward unreddened stars. The direction of this motion is indicated by the dashed straight lines whose slope corresponds to the ratio $E(J-K)/E(J-H)$ under the assumption of a standard extinction law (Cardelli et al. 1989).

The separation between the lines corresponds to the uncertainty of the measured colors of the source. Only the stars lying within the dashed lines can be the source companions. We see from the

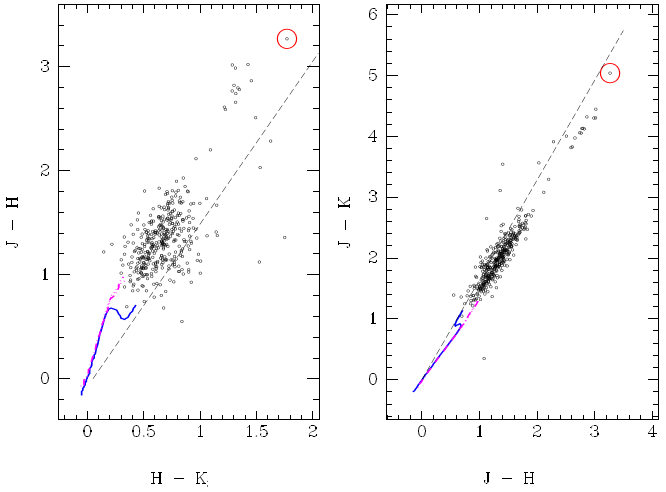

Figure 12. Near-IR color–color diagrams of the 80″ region observed in *JHK*. The target is circled (red). The loci of main-sequence stars are shown as solid blue curves, while those of giants and supergiants are shown as dotted and dotted–dashed pink curves (they overlap). The extinction vector of an A0 star is shown as a dashed line.

figure that only the red giants of late K or M classes are eligible to be a real companion of XTE J1858+034. At the same time, early classes of giants or supergiants can be excluded according to this diagram.

As was previously shown, if the counterpart of XTE J1858 +034 is indeed a red giant star, the magnitude of the absorption toward the source is $A_K \simeq (2.6–3.0)$. Using these values for the extinction correction of the observed colors, we can additionally restrict the class of possible source companions (violet dashed polygon in Figure 11).

Summarizing all of the above, we can conclude that the most likely optical counterpart of the source is a K-M red giant located at a distance of 7–14 kpc. It is worth noting that such a significant distance to the system is supported by the X-ray timing analysis performed by Malacaria et al. (2021), whose estimate is $d \sim 10.9$ kpc.

The same conclusion can be reached using a slightly different approach to the analysis and interpretation of photometric measurements. The *JHK* photometry of point sources in the $80'' \times 80''$ field of view of the NOTCam high-resolution camera in the $J-H/H-K$ and $J-K/J-H$ color–color diagrams is shown in Figure 12. In both diagrams, the intrinsic colors of main-sequence stars are shown as a solid blue curve, while those of giants (dotted pink curve) and supergiants (dotted–dashed pink curve) are taken from Koornneef (1983). Giants and supergiants overlap, but both clearly separate from the main-sequence stars at late spectral types. The reddening vector is plotted for an A0 star as a dashed line based on a standard interstellar extinction law (Cardelli et al. 1989). The target is the circled dot, one of the reddest objects detected in all three filters. We see that the target seems to follow the trace of a highly reddened late-type giant or supergiant, and its location does not fit an early-type reddened star. The photometry clearly supports the spectroscopic suggestion of a K or M giant or supergiant. The intrinsic $H-K$ color is in the small range from 0.12 to 0.35 mag from K0 to M6 stars according to Koornneef (1983) and Wegner (2014). The two extremes give $E(H-K) = (H-K)_{\rm obs} - (H-K)_{\rm int}$ from 1.42 to 1.65 mag, which translates to extinction estimates of A_K in the range from 2.5 to 2.9 mag. This gives a dereddened K-band magnitude in the range from 10.6 to 11.0 mag. The different spectral types have

different absolute K-band magnitudes, resulting in a range of distances from 7 to 14 kpc for K-M giants, while for supergiants, the distance is even larger.

4.3. Previously Proposed Companions

At least two different stars were earlier considered as a possible companion of XTE J1858+034 (Reig et al. 2005; Malacaria et al. 2020). The first star was discussed above and is the only one in the nearby vicinity of XTE J1858+034 (see Figure 6, marked by a plus sign) whose optical spectrum shows Hα emission. Reig et al. (2005) suggested that this object was a Be star and a possible counterpart of XTE J1858+034. It is important to note that the coordinates of this star reported by Reig et al. (2005) are approximately 6″ away from another X-ray object, registered by Chandra inside the INTEGRAL/IBIS error circle (marked with the number 2 in Figure 6, coordinates R.A. $= 18^{h}58^{m}35\overset{s}{.}62$, decl. $= 3°26'10\overset{''}{.}5$; Skiff 2014). We checked Pan-STARRS and Gaia data and found that there is only one optical star coinciding exactly with the Chandra source number 2. Its magnitudes in optical filters are similar to the ones reported by Reig et al. (2005). These facts allow us to suggest that this star and the star reported by Reig et al. (2005) are the same object. The Gaia data indicate that it is located at a distance of $\simeq$200 pc (Bailer-Jones et al. 2018) and has an effective temperature of $T_{\rm eff} \simeq 4000$ K (Gaia Collaboration et al. 2018). These measurements, as well as the registration of the Hα emission line by Reig et al. (2005), indicate that it can be a nearby cataclysmic variable.

Another optical companion of XTE J1858+034 was considered by Malacaria et al. (2020) from the Gaia catalog as the closest star to the nominal source position known at that moment (marked by a cross in Figure 7). Based on the above analysis, this hypothesis can now be firmly ruled out as well.

5. Conclusion

In this work, we present the results of the spectral and temporal analysis of a poorly studied XRP, XTE J1858+034, performed in a broad range of energies and mass accretion rates. The spectrum of the source obtained with the NuSTAR observatory during an outburst in 2019 revealed the presence of a cyclotron absorption line in the energy spectrum at $E_{\rm cyc} \simeq 48$ keV that allowed us to estimate the NS magnetic field strength as 5.2×10^{12} G. The spectral properties of XTE J1858+034 observed by the XMM-Newton and Chandra observatories in the quiescent state point to ongoing accretion in this state, which we interpreted as accretion from the cold (low-ionization) accretion disk.

Chandra data allowed us to obtain the precise localization of XTE J1858+034 for the first time. Observations at the NOT revealed only one potential near-IR companion of the pulsar. The spectral properties of the counterpart point to the red giant star located at 7–14 kpc, suggesting that the system is likely a symbiotic binary hosting an XRP rather than a Be X-ray binary, as previously proposed. This distance agrees well with estimates obtained from the timing properties of the pulsar (Malacaria et al. 2021).

This work was supported by grant 19-12-00423 of the Russian Science Foundation. Studies partially based on observations made with the Nordic Optical Telescope, owned in collaboration by the University of Turku and Aarhus University and operated jointly by Aarhus University, the University of Turku, and the University of Oslo, representing Denmark, Finland, and Norway, the University of Iceland and Stockholm University at the Observatorio del Roque de los Muchachos, La Palma, Spain, of the Instituto de Astrofisica de Canarias.

ORCID iDs

Sergey S. Tsygankov https://orcid.org/0000-0002-9679-0793
Alexander A. Lutovinov https://orcid.org/0000-0002-6255-9972
Sergey V. Molkov https://orcid.org/0000-0002-5983-5788
Anlaug A. Djupvik https://orcid.org/0000-0001-6316-9880
Victor Doroshenko https://orcid.org/0000-0001-8162-1105
Alexander A. Mushtukov https://orcid.org/0000-0003-2306-419X
Christian Malacaria https://orcid.org/0000-0002-0380-0041
Peter Kretschmar https://orcid.org/0000-0001-9840-2048
Juri Poutanen https://orcid.org/0000-0002-0983-0049

References

Anders, E., & Grevesse, N. 1989, GeCoA, 53, 197
Arnaud, K. A. 1996, in ASP Conf. Ser. 101, Astronomical Data Analysis Software and Systems V, ed. G. H. Jacoby & J. Barnes (San Francisco, CA: ASP), 17
Bailer-Jones, C. A. L., Rybizki, J., Fouesneau, M., Mantelet, G., & Andrae, R. 2018, AJ, 156, 58
Basko, M. M., & Sunyaev, R. A. 1975, A&A, 42, 311
Boldin, P. A., Tsygankov, S. S., & Lutovinov, A. A. 2013, AstL, 39, 375
Cardelli, J. A., Clayton, G. C., & Mathis, J. S. 1989, ApJ, 345, 245
Daugherty, J. K., & Harding, A. K. 1986, ApJ, 309, 362
Davies, B., Figer, D. F., Kudritzki, R.-P., et al. 2007, ApJ, 671, 781
Djupvik, A. A., & Andersen, J. 2010, in Highlights of Spanish Astrophysics V, ed. J. Diego et al. (Berlin: Springer), 211
Doroshenko, V., Tsygankov, S. S., Mushtukov, A. A., et al. 2017, MNRAS, 466, 2143
Doroshenko, V. A., Doroshenko, R. F., Postnov, K. A., Cherepashchuk, A. M., & Tsygankov, S. S. 2008, ARep, 52, 138
Filippova, E. V., Tsygankov, S. S., Lutovinov, A. A., & Sunyaev, R. A. 2005, AstL, 31, 729
Gaia Collaboration, Brown, A. G. A., Vallenari, A., et al. 2018, A&A, 616, A1
Garmire, G. P., Bautz, M. W., Ford, P. G., & Nousek, J. A. 2003, Proc. SPIE, 4851, 28
Güver, T., & Özel, F. 2009, MNRAS, 400, 2050
Harrison, F. A., Craig, W. W., Christensen, F. E., et al. 2013, ApJ, 770, 103
Herold, H. 1979, PhRvD, 19, 2868
Karasev, D. I., Lutovinov, A. A., Revnivtsev, M. G., & Krivonos, R. A. 2012, AstL, 38, 629
Koornneef, J. 1983, A&A, 500, 247
Krimm, H. A., Holland, S. T., Corbet, R. H. D., et al. 2013, ApJS, 209, 14
Leahy, D. A. 1987, A&A, 180, 275
Lutovinov, A. A., & Tsygankov, S. S. 2009, AstL, 35, 433
Malacaria, C., Jenke, P., Roberts, O. J., et al. 2020, ApJ, 896, 90
Malacaria, C., Kretschmar, P., Madsen, K. K., et al. 2021, ApJ, 909, 153
Marshall, F. E., Chakrabarty, D., & Finger, M. H. 1998, IAUC, 6828, 2
Molkov, S. V., Cherepashchuk, A. M., Revnivtsev, M. G., et al. 2004, ATel, 274, 1
Mushtukov, A. A., Suleimanov, V. F., Tsygankov, S. S., & Poutanen, J. 2015a, MNRAS, 447, 1847
Mushtukov, A. A., Tsygankov, S. S., Serber, A. V., Suleimanov, V. F., & Poutanen, J. 2015b, MNRAS, 454, 2714
Nakajima, M., Mihara, T., & Makishima, K. 2010, ApJ, 710, 1755
Nakajima, M., Negoro, H., Kurogi, K., et al. 2019, ATel, 13217, 1
Paul, B., & Rao, A. R. 1998, A&A, 337, 815
Predehl, P., & Schmitt, J. H. M. M. 1995, A&A, 293, 889
Reig, P., Negueruela, I., Papamastorakis, G., Manousakis, A., & Kougentakis, T. 2005, A&A, 440, 637
Remillard, R., Levine, A., Takeshima, T., et al. 1998, IAUC, 6826, 2
Skiff, B. A. 2014, yCat, 1, 2023
Staubert, R., Trümper, J., Kendziorra, E., et al. 2019, A&A, 622, A61

Takeshima, T., Corbet, R. H. D., Marshall, F. E., Swank, J., & Chakrabarty, D. 1998, IAUC, 6826, 1
Tsygankov, S. S., Mushtukov, A. A., Suleimanov, V. F., et al. 2017a, A&A, 608, A17
Tsygankov, S. S., Wijnands, R., Lutovinov, A. A., Degenaar, N., & Poutanen, J. 2017b, MNRAS, 470, 126
van Leeuwen, F. 2007, A&A, 474, 653
Wachter, K., Leach, R., & Kellogg, E. 1979, ApJ, 230, 274
Wallace, L., & Hinkle, K. 1997, ApJS, 111, 445
Wegner, W. 2000, MNRAS, 319, 771
Wegner, W. 2006, MNRAS, 371, 185
Wegner, W. 2007, MNRAS, 374, 1549
Wegner, W. 2014, AcA, 64, 261
Wegner, W. 2015, AN, 336, 159